Available online at www.sciencedirect.com
ScienceDirect
Thin Solid Films 515 (2007) 5298–5307
www.elsevier.com/locate/tsf

# Chemical vapor deposition of amorphous ruthenium–phosphorus alloy films

Jinhong Shin [a], Abdul Waheed [b,1], Wyatt A. Winkenwerder [c], Hyun-Woo Kim [c], Kyriacos Agapiou [b], Richard A. Jones [b], Gyeong S. Hwang [c], John G. Ekerdt [c,*]

[a] Texas Materials Institute, University of Texas at Austin, Austin, TX 78750, USA
[b] Department of Chemistry and Biochemistry, University of Texas at Austin, Austin, TX 78712, USA
[c] Department of Chemical Engineering, University of Texas at Austin, Austin, TX 78712, USA

Received 13 October 2006; received in revised form 5 December 2006; accepted 2 January 2007
Available online 12 January 2007

**Abstract**

Chemical vapor deposition growth of amorphous ruthenium–phosphorus films on $SiO_2$ containing ~15% phosphorus is reported. *cis*-Ruthenium(II)dihydridotetrakis-(trimethylphosphine), *cis*-$RuH_2(PMe_3)_4$ (Me=$CH_3$) was used at growth temperatures ranging from 525 to 575 K. Both Ru and P are zero-valent. The films are metastable, becoming increasingly more polycrystalline upon annealing to 775 and 975 K. Surface studies illustrate that demethylation is quite efficient near 560 K. Precursor adsorption at 135 K or 210 K and heating reveal the precursor undergoes a complex decomposition process in which the hydride and trimethylphosphine ligands are lost at temperatures as low at 280 K. Phosphorus and its manner of incorporation appear responsible for the amorphous-like character. Molecular dynamics simulations are presented to suggest the local structure in the films and the causes for phosphorus stabilizing the amorphous phase.


*Keywords:* Amorphous films; Ruthenium alloy; Chemical vapor deposition; *Ab initio* molecular dynamics simulation

## 1. Introduction

For decades, ultra-large-scale integrated microelectronic devices have been continuously improved in functionality, operating speed and circuit density, and this has led to the use of Cu-based interconnects. While Cu provides several advantages, such as lower resistivity and higher electromigration resistance, than the Al metal it displaced, a diffusion barrier is needed since Cu readily diffuses into silicon to either act as an impurity or to form a silicide. Currently, Ta or a TaN/Ta multilayer stack is deposited by physical vapor deposition (PVD) on an interlayer dielectric as the Cu diffusion barrier, and then a Cu seed layer is deposited on the Ta for subsequent Cu electroplating [1]. However, the PVD technology used to grow Ta or the TaN/Ta multilayer stack may not be extendable to the 32-nm generation of devices and beyond where an ultra-thin (<3 nm) and conformal barrier/cladding layer multilayer stack is required to maintain a low effective interconnect resistivity [2]. This has motivated studies on new barrier/cladding layer materials including $TiSi_xN_y$ [3], $WN_xC_y$ [4] and Ru [5–9], and on alternate deposition technologies, such as chemical vapor deposition (CVD) and atomic layer deposition (ALD).

Ruthenium has been considered for a number of microelectronics applications, including use as a Cu diffusion barrier and Cu seed layer due to its low resistivity (~7 μΩ cm), chemical stability, and low solubility with Cu [5]. However, recent studies point to some barrier limitations of Ru films. For example, a 20 nm Ru film failed to prevent Cu diffusion above 725 K, and a 5 nm Ru film lost its barrier property above only 575 K [10,11]. Ruthenium films can be grown by CVD or ALD methods using precursors such as, Ru carbonyl ($Ru_3(CO)_{12}$) [6], cyclopentadienyl derivatives such as $Cp_2Ru$ [7] or $(EtCp)_2Ru$ [8], and β-diketonates such as $Ru(thd)_3$ [9], (Cp=$\eta^5$-$C_5H_5$, Et=$C_2H_5$, EtCp=$\eta^5$-$C_5H_4Et$, thd=2,2,6,6-tetramethyl-3,5-heptanedione). In general, Ru films deposited by CVD or PVD methods follow a 3D, Volmer–Weber growth mechanism, due

* Corresponding author. Tel.: +1 512 471 4689; fax: +1 512 471 7060.
*E-mail address:* ekerdt@che.utexas.edu (J.G. Ekerdt).
[1] Current address: Department of Chemistry, Virginia Tech, Blacksburg, VA 24060 USA.

0040-6090/$ - see front matter © 2007 Elsevier B.V. All rights reserved.
doi:10.1016/j.tsf.2007.01.002

to its high surface energy ($\gamma_{Ru(001)}$=3.05 J/m$^2$) [12] and this leads to polycrystalline, columnar films. Fast Cu diffusion can occur through grain boundaries due to the much higher diffusion at grain boundaries than in the bulk [13]. If the poor barrier capability of thin Ru films is rooted in their columnar structure, controlling the microstructure of Ru films is essential in improving barrier properties. Changing the Ru film microstructure from polycrystalline to nanocrystalline or from polycrystalline to amorphous should eliminate or suppress the fast diffusion of Cu through grain boundaries.

Herein we report the CVD growth of nearly amorphous Ru–P alloy metal films by employing *cis*-$RuH_2(PMe_3)_4$ (Me=$CH_3$) as the precursor. Amorphous metallic alloy films and powders grown by plasma enhanced-ALD, PVD, CVD, reduction of metal ions in solution, or electroless deposition have been reported for $TaN_x$, Ta–Ru–N, FeB, $NiP_x$, $NiB_x$, and $CoW_xP_y$ [14–18]. Studies have shown these films to be metastable and undergo crystallization at high annealing temperatures [14,16–18]. Much can likely be learned about the structure, formation driving forces, and stability of the amorphous metal alloy films from the literature on bulk metallic glasses [19–24]. To that end, and borrowing from the approaches applied to bulk metallic glasses, we also report *ab initio* molecular dynamics simulations that provide insight into the local structure of amorphous Ru–P alloys. The first principles approach [24] has allowed us not only to establish a realistic description of glassy structures but also to develop a detailed understanding of the origin of short-to-medium-range order often seen in amorphous alloy structures.

## 2. Methods

Film growth was carried out in a deposition and analysis facility consisting of a vacuum sample transfer system, load lock, X-ray photoelectron spectroscopy (XPS) system (Physical Electronics 3057; Mg Kα), CVD chamber, and a PVD chamber equipped with direct current magnetron sputtering. The stainless steel CVD chamber is a cold-wall vessel (base pressure $6.7\times10^{-6}$ Pa) and the $SiO_2$/Si(100) substrates were heated radiatively from below. Thermally grown $SiO_2$ (100 nm)/Si(100) 200 mm wafers were supplied by Sematech. The wafers were cut into 20×20 mm pieces and heated to the growth temperature under vacuum. *cis*-$RuH_2(PMe_3)_4$ was synthesized according to procedures described below; the solid compound was sublimed at 353 K to obtain sufficient vapor pressure and delivered to the CVD chamber using flowing Ar through a heated gas line and shower head. The deposition was carried out at ~26.7 Pa. *Ex situ* XPS chemical state analysis was performed with a Physical Electronics 5700, which is fitted with a monochromatic Al Kα source. Crystallinity is established using grazing angle (2°) X-ray diffraction (XRD) (Bruker-Nonius D8), cross section transmission electron microscopy (TEM) (JOEL 2010F operated at 200 keV) and selected area diffraction (SAD).

The precursor, *cis*-$RuH_2(PMe_3)_4$, was prepared by a modification of the published procedure from *trans*-$RuCl_2(PMe_3)_4$ and the intermediate borohydride derivative [25,26].

### 2.1. General

All reactions were performed under a dry, oxygen-free nitrogen atmosphere or under vacuum using standard Schlenk line and dry box techniques. Solvents were dried prior to use by distillation from $CaH_2$. Sodium borohydride was purchased from Fisher Scientific and dried under vacuum overnight prior to use. Trimethylphosphine (97%) was purchased from Aldrich and used without further purification.

### 2.2. Preparation of *trans*-$RuCl_2(PMe_3)_4$

Trimethylphosphine (4.5 g, 60 mmol) was added to a stirred solution of $RuCl_3\times H_2O$ (2.7 g, 13 mmol) in methanol (30 mL) at 298 K. The mixture was stirred (18 h) at 298 K during which time a yellow precipitate formed. The solid was isolated by filtration, then dried under vacuum, and used in the next step without further purification. (Isolated: *trans*-$RuCl_2(PCH_3)_4$, 3.8 g, 81% as a greenish yellow solid, m.p. 503–510 K, (dec. 462–466 K).

### 2.3. Preparation of *mer*-$(PMe_3)_3RuH(\eta^2\text{-}H_2BH_2)$

Methanol (1.0 to 1.5 mL) was added dropwise, slowly until violent gas evolution was observed to a stirred mixture of *trans*-$RuCl_2(PMe_3)_4$ (1.1 g, 2.3 mmol) and sodium borohydride (730 mg, 19 mmol) in benzene (70 mL) at 298 K. The mixture was stirred (2 h) at 298 K after which the solvent was removed under vacuum. The brown residue was extracted with hexane, and filtered through a short bed of Celite®. The filtrate was evaporated to dryness under vacuum to give a bright yellow solid. (Isolated: *mer*-$(PMe_3)_3RuH(\eta^2\text{-}H_2BH_2)$, 650 mg, 82% as a bright yellow solid, m.p. 378–381 K.

### 2.4. Preparation of *cis*-$RuH_2(PMe_3)_4$ (1)

Trimethylphosphine (460 mg, 6 mmol) was added dropwise to a stirred solution of *mer*-$(PMe_3)_3RuH(\eta^2\text{-}H_2BH_2)$ (1.04 g, 3 mmol) in benzene (80 mL) at 298 K. The yellow mixture was stirred at 298 K until it was nearly colorless (faintly brown after 1 h), then the solvent was evaporated under vacuum. The crude, light brown solid was sublimed (353 K, 1.3 Pa) onto a 195 K cold probe. Isolated 1: 740 mg, 86% as a white solid.

The surface science study was conducted in an ultra-high vacuum chamber equipped with a cryogenic pump to maintain a base pressure of $6.9\times10^{-8}$ Pa during XPS analysis and a diffusion pump that maintains a base pressure of $1.5\times10^{-7}$ Pa for precursor dosing and temperature programmed desorption (TPD). TPD and XPS were done *in situ* on an Extrel C50 quadrapole mass spectrometer and a PHI 5000C ESCA system, respectively. *cis*-$RuH_2(PMe_3)_4$ was heated to 353 K while the stainless steel tubing and valves were heated to 363 K to prevent deposition in dosing lines. *cis*-$RuH_2(PMe_3)_4$ was introduced into the chamber using an uncalibrated, pin-hole doser, and dosed onto a polycrystalline tantalum foil heated resistively and cooled by liquid nitrogen. XPS peaks are shifted to give C 1s at 285.0 eV. The tantalum foil contained small amounts of oxygen

that could not be removed by heating, annealing or ion sputtering and is referred to herein as a sub-oxide ($Ta_xO_y$) foil. The sample was regenerated using an $Ar^+$ ion gun to remove any Ru that was deposited and annealed to 1275 K to heal the ion damage.

For the construction of model amorphous Ru–P alloy structures used in our theoretical analysis, we began by randomizing Ru in a periodic supercell and then replaced a given fraction of Ru with P. Next, the alloy was melted at high temperatures (3500 K) for 3 picoseconds (ps) with a time step of 1 femtosecond (fs), using *ab initio* molecular dynamics (MD) within a Born–Oppenheimer framework, and then quenched to 500 K at a rate of 1.5 K/fs, followed by static structural optimization. Here the temperature was controlled using velocity rescaling.

Our *ab initio* MD simulations were performed within the generalized gradient approximation plane-wave 91(GGA-PW91) [27] to density functional theory (DFT) using the well established Vienna *ab initio* Simulation Package [28–30]. A plane-wave basis set for valence electron states and Vanderbilt ultrasoft pseudopotentials for core-electron interactions were employed. A plane-wave cutoff energy of 300 eV was used and the Brillouin zone integration was performed using one k-point (at Gamma). The $Ru_{80}P_{20}$ amorphous alloy system reported herein was modeled using a periodic 144-atom supercell (consisting of 115 Ru and 29 P atoms) with an optimized volume of 2 $nm^3$ at 0 K. While no simulation study has been reported for the Ru–P system, our $Ni_{80}P_{20}$ structure obtained using the same procedure shows excellent agreement with that from previous extensive *ab initio* MD simulations [24]. This confirms the soundness of our approach.

## 3. Results

### 3.1. Film growth studies

The precursor is a solid that sublimes intact at temperatures as high as 405 K. Fig. 1 presents mass sweeps of the vapor space above the precursor as it was heated from room temperature to

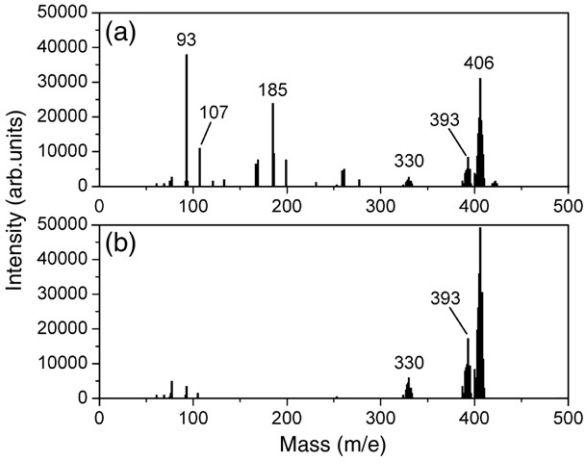


Fig. 1. Electron impact ionization analysis of the vapor produced during sublimation at (a) 345 K and (b) 405 K.

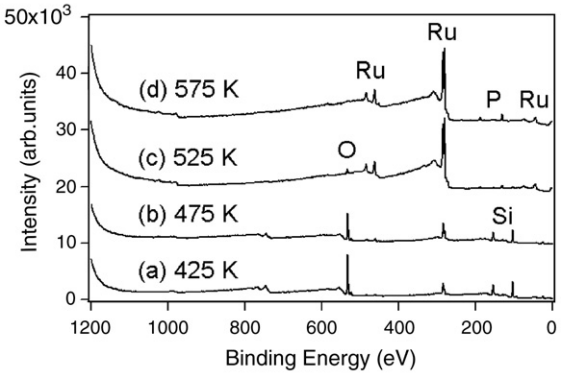


Fig. 2. XPS survey scan results of the Ru films deposited with *cis*-$RuH_2(PMe_3)_4$ at different substrate temperatures: (a) 425 K, (b) 475 K, (c) 525 K, and (d) 575 K.

405 K. *cis*-$RuH_2(PMe_3)_4$ has a molecular weight of 407 and the appearance of fragmentation peaks at 345 K and 405 K for masses 406, 393 and 330 are indicative of the compound. The additional peak for masses 93, 107, and 185 are contaminants associated with synthesis. *cis*-$RuH_2(PMe_3)_4$ was heated to 353 K during growth.

Film growth was possible above 525 K. The XPS survey scans in Fig. 2 show the films contain Ru and P. The Si (104.3 eV) and O (533.5 eV) features are associated with the 100 nm thick thermal oxide/Si(100) substrate. Under the conditions of our growth (1 h, 26.7 Pa pressure, dosing geometry) a continuous film was not realized at 525 K, and a continuous 30 nm Ru film (see below) grew at 575 K. The chemical state of Ru is metallic for the films grown at 525 and 575 K, as indicated by the binding energy of the Ru $3d_{5/2}$ peak at 280.0 eV. A weak Ru $3d_{5/2}$ peak that is not apparent in Fig. 2 is present at 281.2 eV for the 475 K film, which is attributed to Ru in adsorbed or partially decomposed precursor molecules. Fig. 3 shows XPS depth profile results of the films deposited at 525 and 575 K, indicating that higher substrate temperatures resulted in a higher P concentration and that both films have higher P concentrations near the film surface than in the bulk. The P concentrations near the surface are 13% and 28% for the 525 K and 575 K films, respectively, and continuously decrease with sputtering. The P concentration of the 525 K film dropped to near zero after 45 s of sputtering as the film was removed, while the 575 K film shows ~15% of P concentration after 105 s of sputtering. (The O and Si signals in Fig. 3a are associated with the $SiO_2$ because the film was not continuous.) The cause(s) for a P profile were not revealed in this study; there may be a surface enrichment associated with cooling the sample in the growth chamber to 325 K, during which time residual precursor and precursor decomposition products can adsorb on the surface.

Fig. 4 shows high resolution Ru 3d and P 2p XPS peaks for the film deposited at 575 K. Because of the overlapping Ru $3d_{3/2}$ and C 1s peaks, the C content cannot be obtained directly from XPS measurements. However, the intensity ratio of the 3d doublet peaks is 1.5 for the 575 K film, which is close to the theoretical value for pure Ru, indicating that the film contains

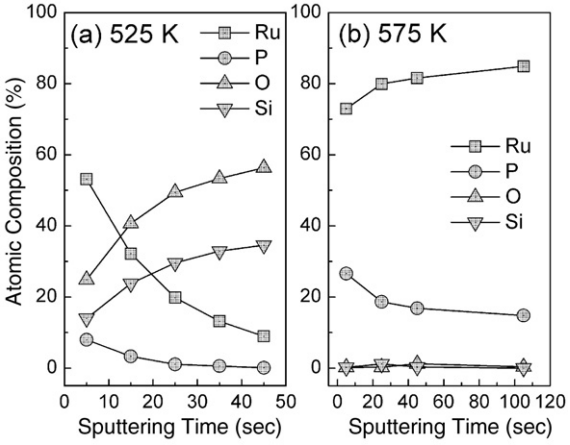


Fig. 3. XPS depth profiles of the atomic concentrations of the Ru films grown at (a) 525 K and (b) 575 K.

<1% of C [31]. The P $2p_{3/2}$ peak at 129.8 eV indicates P is present in the zero-valent state and is not donating or accepting electrons with Ru [32]. The 525 K film also has a P $2p_{3/2}$ peak at 129.8 eV.

The surface morphology of a 30 nm thick Ru–P film deposited at 575 K was inspected by scanning electron microscopy and the micrographs (not shown) reveal a smooth surface without observable grain boundaries. Atomic force microscopy measurements of this film lead to a root-mean-square (RMS) roughness of 0.52 nm. For comparison a 3.5 nm PVD Ru film has a 0.11 nm RMS roughness, and the $SiO_2$/Si (001) substrate has a 0.20 nm roughness. The smooth surface of the 575 K-CVD film can be seen in the cross section TEM image in Fig. 5a and contrasted against the PVD film.

Grazing angle XRD results for a 575 K-CVD film, 30 and 5 nm PVD films, and a 30 nm Ru film grown by thermal CVD at 525 K from (2,4-dimethylpentadienyl)$_2$Ru are presented in Fig. 6. The PVD films and an additional CVD film were examined to ensure the grazing angle technique would be sensitive enough for ultra-thin films. The 30 nm CVD film deposited with (2,4-dimethylpentadienyl)$_2$Ru and the 20 nm thick PVD film show

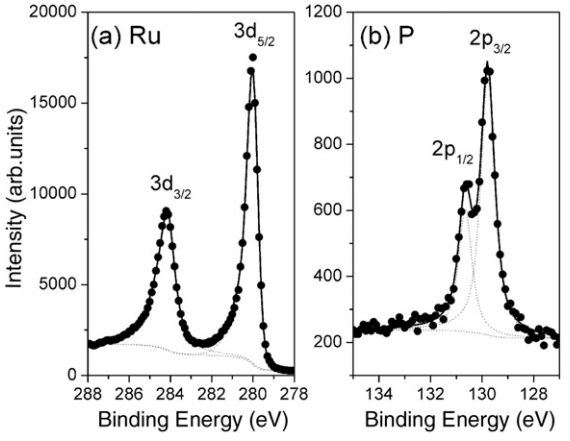


Fig. 4. High resolution XPS result of the (a) Ru 3d and (b) P 2p peaks for a film deposited at 575 K.

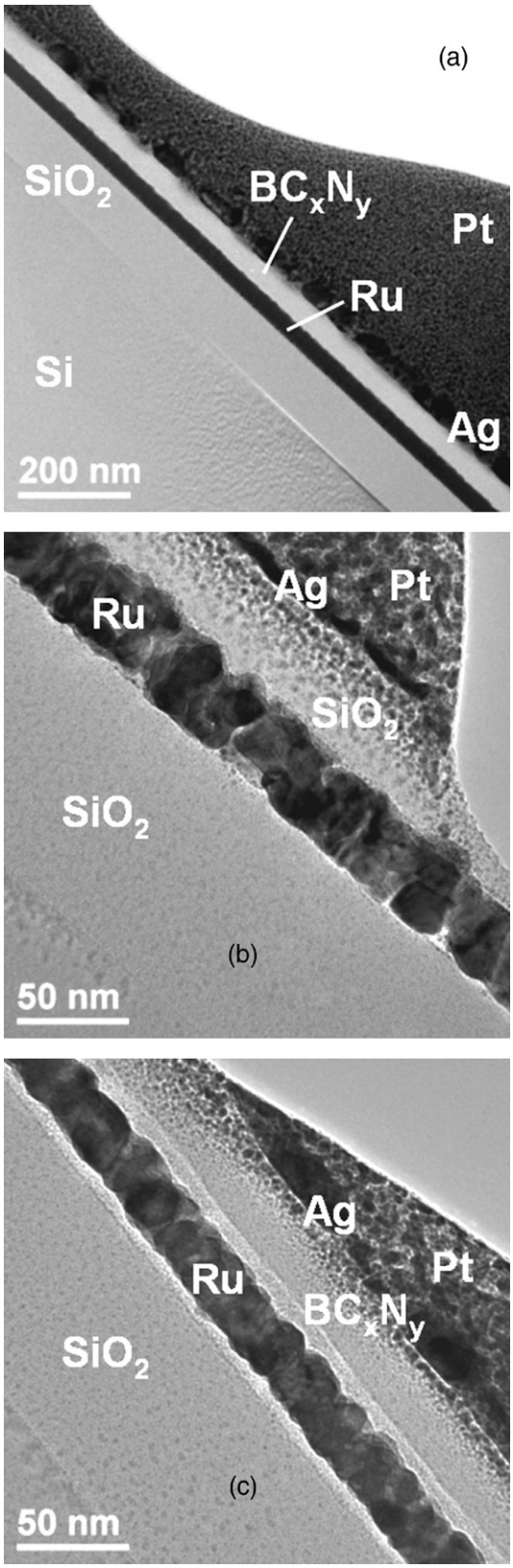


Fig. 5. Cross section TEM of: (a) the Ru–P film grown by CVD at 575 K, (b) a 30 nm PVD Ru film, and (c) the Ru–P film grown at 575 K and annealed to 975 K for 30 min.

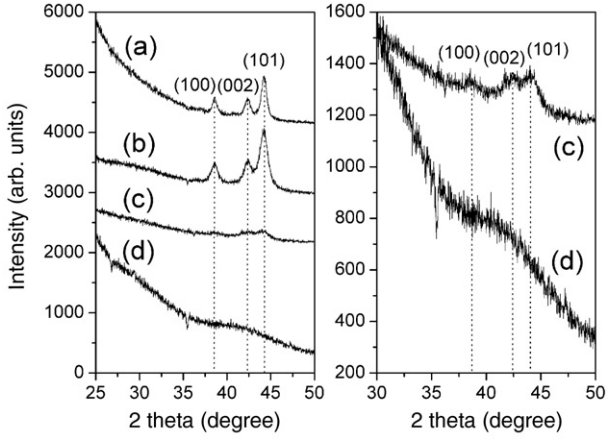


Fig. 6. XRD of Ru films: (a) 20 nm PVD Ru, (b) 30 nm CVD Ru deposited with $Ru(C_7H_{11})_2$, (c) 5 nm PVD Ru, and (d) 30 nm CVD Ru–P deposited with *cis*-$RuH_2(PMe_3)_4$.

clear peaks at $2\theta = 38.6°$, 42.4°, and 44.2°, which represent the (100), (002), and (101) planes of the hexagonal close packed Ru lattice, respectively [33]. The 5 nm PVD film also shows peaks at the same positions that indicate the film is polycrystalline Ru, although the peaks are quite weak due to its low thickness. In contrast, no peak was observed for the film grown with *cis*-$RuH_2(PMe_3)_4$, suggesting that the film is amorphous or has nanocrystallites that are too small to be detected by XRD; i.e., an XRD-level amorphous film [34].

The microstructure of the Ru–P film deposited at 575 K was also analyzed using dark field TEM (Fig. 7) and SAD pattern measurement (Fig. 8(b)). Note the TEM sample preparation involves coating the CVD Ru film with a $BC_xN_y$ film in a process that takes 3 h at 635 K. Generally, Ru films deposited by a CVD or PVD method are polycrystalline having columnar structures, however the films grown with *cis*-$RuH_2(PMe_3)_4$ show a significantly different microstructure. The SAD pattern (Fig. 8(b)) does not feature a sharp ring or spot pattern, while the PVD film pattern (Fig. 8(a)) has a well-developed spot pattern. The sharp spot pattern is expected for the PVD film based on the XRD results (Fig. 6) and separate TEM images (not shown). A diffuse ring pattern can be observed from films composed of extremely small crystallites, which cause overlapping of crystalline diffraction lines with broadening, or can be observed from amorphous films having a random microstructure [35]. The criteria and transition between the two cases (i.e., nanocrystalline versus amorphous) are not clear because amorphous microstructures have some degree of local order. The Ru–P film deposited with *cis*-$RuH_2(PMe_3)_4$ shows an amorphous-like random microstructure, however small crystallites a few nm in size were observed, especially near the $SiO_2$ substrate rather than near the film surface.

The Ru–P alloy films are metastable and become increasingly more crystalline upon annealing to 775 or 975 K. Fig. 9 presents the dark field TEM image of the 575 K-CVD film after it was annealed in vacuum to 775 K for 30 min. Fig. 5c presents a cross section of the film after annealing to 975 K. The SAD patterns in Fig. 8 illustrate the appearance of definite spots at 775 K and then well-developed spots at 975 K. Most of the film adjacent to the $SiO_2$ substrate appears polycrystalline in Fig. 9. The small crystallites that formed during deposition at 575 K (Fig. 7) could have acted as nuclei for crystallite growth upon annealing to 775 K. The TEM image in Fig. 5 demonstrates the polycrystalline film has a large grain structure after annealing to 975 K. Chemical mapping studies using electron energy loss spectroscopy were not performed to determine if there was any segregation of the P under high temperature annealing.

### 3.2. Surface studies

A 5.9 Langmuir (L) dose of *cis*-$RuH_2(PMe_3)_4$ was delivered to a $Ta_xO_y$ surface heated at 455 K. The Ru $3d_{3/2}$ and C 1s

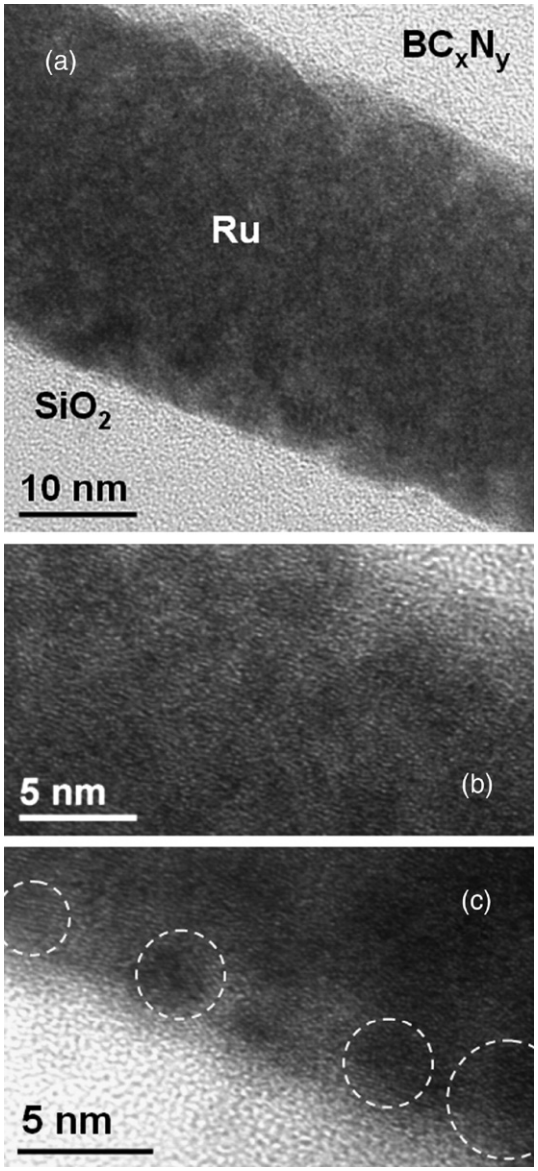


Fig. 7. Dark field TEM image of the 30 nm CVD Ru–P film deposited with *cis*-$RuH_2(PMe_3)_4$ at 575 K for 1 h. The circles are drawn to indicate where crystalline regions are detected. Panel (a) presents the cross section of the entire sample and Panels (b) and (c) present close up views of the Ru–P film near the growth surface and at the $SiO_2$ substrate, respectively.

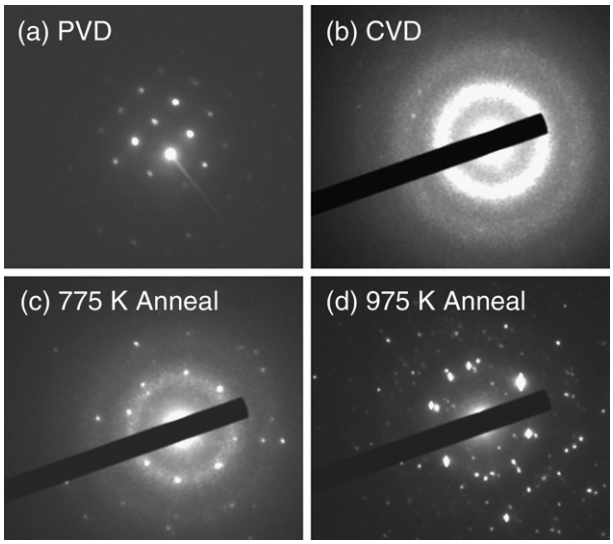


Fig. 8. SAD patterns of (a) a PVD Ru film, (b) a CVD Ru–P film grown at 575 K, (c) the Ru–P film annealed to 775 K for 30 min, and (d) the Ru–P film annealed to 975 K for 30 min.

photoelectrons contribute to the broad feature seen at 285 eV in Fig. 10 after dosing, indicating a partially decomposed precursor is present at the surface. The P 2p XPS peaks (not shown), if present, were at the noise level since the Ru 3d electrons are ten times more sensitive than the P 2p electrons in XPS [36] and the signal-to-noise ratio for Ru 3d in Fig. 10 is 4:1. Only the *m*/*e* 15 signal produced a peak at 560 K during TPD. After TPD the 285 eV XPS peak is more narrow, and the Ru $3d_{5/2}$:$3d_{3/2}$ peak ratio is consistent with partial loss of C from the surface. The peak ratio goes from 0.69 before to 0.91 after TPD to 975 K. (Ru containing <1% C has a Ru $3d_{5/2}$:$3d_{3/2}$ peak ratio of 1.5.)

A 0.17 L dose of the precursor was condensed at 135 K and subjected to TPD. Figs. 11 and 12 present the Ru 3d and P 2p signals. The Ru $3d_{5/2}$ feature appears at 280.2 eV and the P 2p signal is centered at 131.5 eV. Note the P $2p_{1/2}$ and $2p_{3/2}$ doublet (Fig. 4) is not resolvable with the *in situ* PHI 5500C system as it does not feature a monochromatic X-ray source. Subsequent TPD of the adsorbed species produces the spectra presented in Fig. 13. Additional masses were monitored, *m*/*e* 46 ($P(CH_3^+)$, 61 ($P(CH_3)_2^+$) and 330 ($RuH_2(P(CH_3)_3^+$) and their signals mirrored the *m*/*e* 406 signal. Features worth noting include: 1) The *m*/*e* 406 signal that is associated with the precursor illustrates molecular desorption; 2) The relative intensity of the *m*/*e* 76:406 signals at 285 K is 189, which is significantly higher than the relative intensity of 0.11 recorded during residual gas analysis of the precursor alone; 3) The relative intensities for *m*/*e* 76, 61, 46, and 31 ($P^+$) are inconsistent with the electron impact ionization fragmentation pattern for $P(CH_3)_3$ [37]; 4) Only the *m*/*e* 16 signal begins to increase at 220 K; and, 5) The relative intensities of the m/e 16:15 signals at 285 K is 0.08, which is different from that associated with $CH_4$, with an intensity ratio of 1.12 [37].

Fig. 14 presents the signal intensities on the high temperature tails of the peaks shown in Fig. 13. The signals have a baseline intensity of zero when a blank surface is ramped to 975 K. *m*/*e* 406 returns to the baseline by 300 K. All the remaining signals continue to generate a nonzero response and m/e 15 and 76 decay differently from m/e 31 and 16. These signals (*m*/*e* 15, 76, 31 and 16) remain essentially at the levels indicated at 350 K up to at least 475 K (not shown). Control experiments verify the nonzero response is not associated with adsorbates desorbing from the sample mounts.

In a separate experiment, 0.018 L of the precursor was adsorbed on the surface at 210 K and annealed to successively higher temperatures for 1.0 min and cooled back to 210 K to collect the XPS signals in Figs. 11 and 12. The Ru $3d_{5/2}$ and P 2p peak positions are the same as found when condensing the precursor at 135 K. The spectra recorded after annealing to 260 K (not shown) were identical in position and intensity to the spectra recorded after dosing. Annealing to 280 K, the leading edge of the molecular desorption feature in Fig. 13, results in attenuation of the Ru $3d_{5/2}$ and P 2p signals. The P 2p signals for

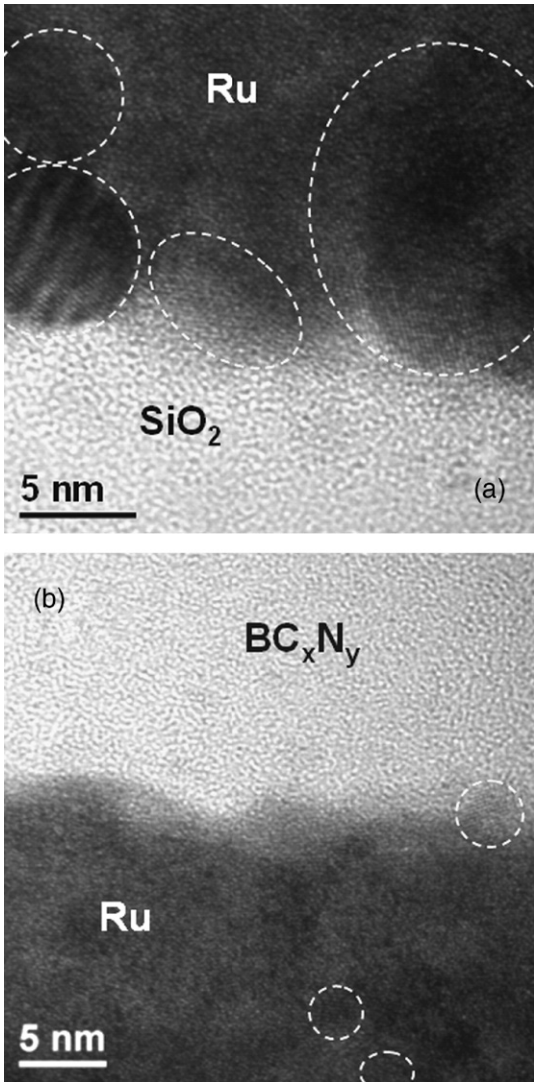


Fig. 9. Dark field TEM image the 30 nm CVD Ru–P film deposited with *cis*-$RuH_2(PMe_3)_4$ 575 K for 1 h and annealed at 775 K for 30 min. The circles are drawn to indicate where crystalline regions are detected. Panel (a) is a view of the film against the $SiO_2$ substrate and Panel (b) is a view near the growth surface.

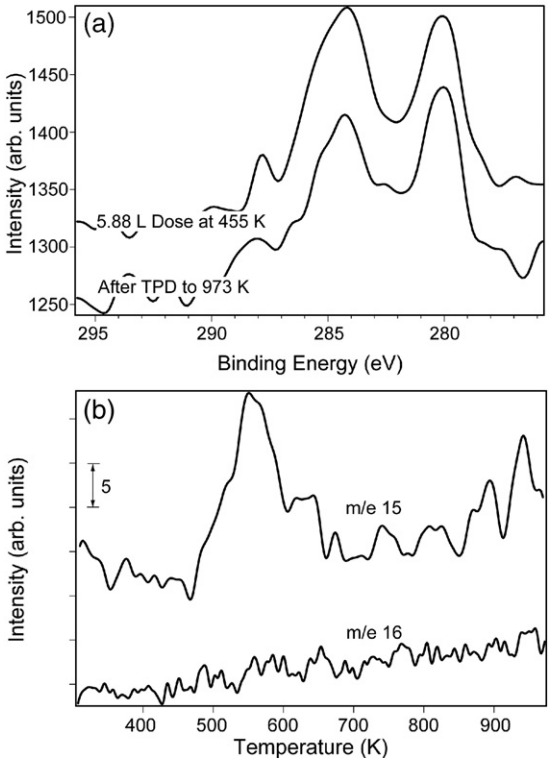


Fig. 10. 6.24 L dose of *cis*-$RuH_2(PMe_3)_4$ at 455 K on $Ta_xO_y$: (a) Ru 3d and C 1s XPS spectra and (b) TPD results.

280 K, 310 K and 410 K anneals are comparable to the noise level; however, the peak does appear to move to lower binding energy for these anneal temperatures. The Ru $3d_{5/2}$ peaks are constant in area, and decreased relative the 280 K anneal, for annealing to 310 and 410 K. The binding energy for the weak $3d_{5/2}$ feature is estimated to be 279.3 eV.

### 3.3. Modeling studies

To understand the nature of local packing in Ru–P amorphous structures, we analyzed various atomic configurations obtained from the melt-quenching molecular dynamics simulations as

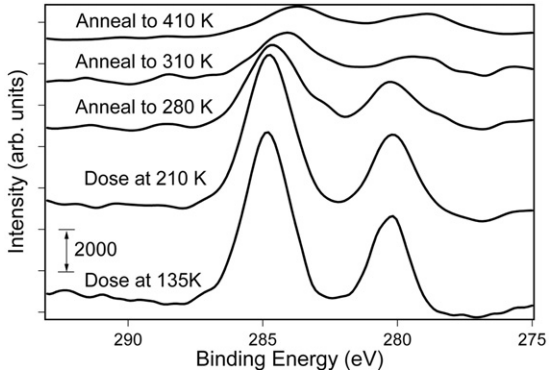


Fig. 11. Ru 3d and C 1s XPS spectra resulting from a 0.17 L dose of *cis*-$RuH_2(PMe_3)_4$ at 135 K, and resulting from a 0.018 L dose of *cis*-$RuH_2(PMe_3)_4$ at 210 K followed by annealing to the indicated temperatures and cooling back to 210 K to record the spectra.

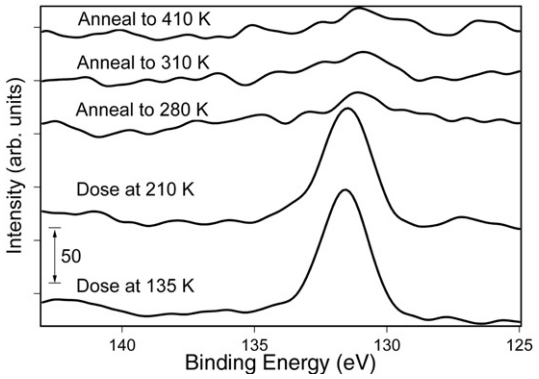


Fig. 12. P 2p XPS spectra resulting from a 0.17 L dose of *cis*-$RuH_2(PMe_3)_4$ at 135 K, and resulting from a 0.018 L dose of *cis*-$RuH_2(PMe_3)_4$ at 210 K followed by annealing to the indicated temperatures and cooling back to 210 K to record the spectra.

described earlier. For the $Ru_{80}P_{20}$ amorphous alloy, as shown in Fig. 15, the solute P atoms are more or less evenly distributed while surrounded by Ru atoms. Our DFT-GGA calculation indeed predicts a negative mixing energy in the amorphous system, implying that unlike bonds are favored. The local structure can be characterized by the nearest-neighbor coordination. For the *ab initio* Ru–P configuration, the average first neighbor coordination number (CN=Z) of the P solute is predicted to be approximately 9.2, with eight Z9 and two Z10 among ten sampled solutes. Here the CN is defined as the number of Ru neighbors of a central P atom within a cutoff distance of 3 Å (obtained from calculated radial-distribution functions), as the first shell of the solute consists of Ru atoms only.

The type of the coordination polyhedron around a solute atom can further be specified using the Voronoi index $<i_3, i_4, i_5, i_6, \ldots>$, where $i_n$ represents the number of $n$-edged faces of the Voronoi polyhedron [38,39]. In the $Ru_{80}P_{20}$ glass, the dominant Kasper polyhedra with CN=9 exhibit <0,3,6,0> and <0,5,4,0> types, where the former appears about four times more than the latter. Fig. 16 shows Z9 and Z10 polyhedra obtained from *ab initio* calculations. In the Ru–P system, seven-edged faces and above were found to hardly occur.

It is now well established that the local order in amorphous binary alloys is strongly controlled by the effective atomic size ratio between solvent and solute atoms, $\lambda$ [23,40,41]. A recent *ab intio* MD study [24] showed that the preferred polyhedra

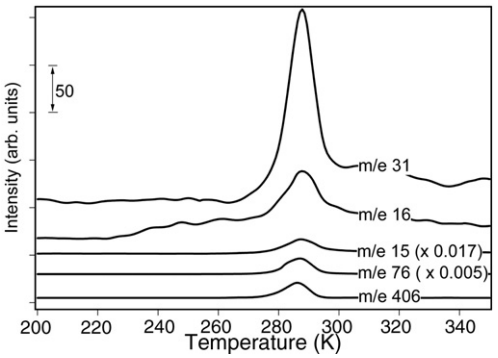


Fig. 13. TPD spectra of the 0.17 L dose of *cis*-$RuH_2(PMe_3)_4$ at 135 K.

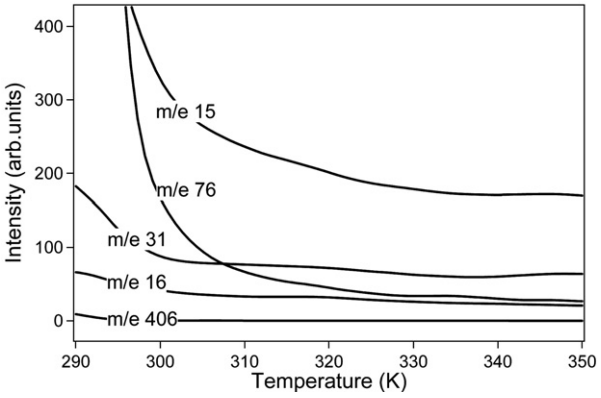


Fig. 14. Trailing edges of the *m*/*e* signals presented in Fig. 13.

type changes with λ; that is, decreasing the atomic size ratio leads to noticeable changes in the structure of polyhedra from icosahedral with Voronoi index <0,0,12,0> ($\lambda \approx 0.90$), to bi-capped square Archimedean antiprism with <0,2,8,0> ($\lambda \approx 0.84$), and then to tri-capped trigonal prism packing (TTP) with <0,3,6,0> ($\lambda \approx 0.73$). Considering the larger atomic size of Ru than Ni by (about 7% in pure metal according to Goldschmidt's rules [19]), we can expect that the atomic size ratio $\lambda$ for the Ru–P alloy is smaller than 0.78 for the Ni–P case. This is consistent with our simulations results showing that the TTP phase is predominant in the $Ru_{80}P_{20}$ structure while the $Ni_{80}P_{20}$ alloy preferably results in the BSAP phase, although the magnitude of $\lambda$ often differs from that evaluated based on Goldschmidt's atomic radii.

As is also shown in Fig. 15, the formation of 'quasi-equivalent' P-centered Ru clusters arising from topological and chemical short-range order is also likely to lead to the medium-range order in the binary alloy, when the clusters are packed in three-dimensional space. In fact, the short-to-medium-range order is seen in other metallic glasses, particularly in transition metal–metalloid and transition metal–transition metal systems where the chemical short-range-order is significant [24].

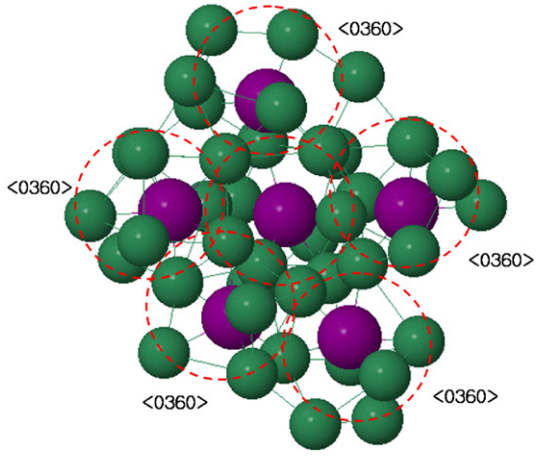


Fig. 15. Modeling results for the packing of the P-centered quasi-equivalent Ru clusters for a $Ru_{80}$:$P_{20}$ mixture. Large (purple) and small (green) balls represent P and Ru atoms, respectively. (For interpretation of the references to color in this figure legend, the reader is referred to the web version of this article).

## 4. Discussion

The TEM, SAD and XRD data illustrate an amorphous Ru–P alloy film can be grown from *cis*-$RuH_2(PMe_3)_4$ in a CVD process at 575 K. The amount of phosphorus changed with depth, decreasing to about 15% within the film bulk. Formation of the amorphous alloy could originate from the uniqueness of the precursor in that it contains both transition metal, Ru, and metalloid, P, or it could result from the physical and chemical effects of mixing alloying components with physical randomization of the lattice due to different atomic sizes and chemical interactions between the metal and metalloid. The modeling studies support the latter.

The surface studies provide insight into the reactions the precursor undergoes during growth. When *cis*-$RuH_2(PMe_3)_4$ is adsorbed above the molecular desorption temperature (285 K), only $CH_3$ is observed to desorb. Sequential demethylation, with retention of P on the surface is likely occurring. Tao et al. followed the reaction of $P(CH_3)_3$ on Ru (0001) and report $P(CH_3)_3$ undergoes stepwise demethylation, with the final step, $P(CH_3) \rightarrow P$, being completed by 500 K [42]. The TPD peak (Fig. 10(b)) could be associated with a similar demethylation reaction only now the $P(CH_3)_y$ ($y = 1–3$) is bonded to a Ru atom and/or the $Ta_xO_y$ surface. The presence of residual carbon on the $Ta_xO_y$ surface might be explained by some of the demethylation reactions occurring on the Ta surface since Tao et al. ultimately formed $Ru_xP$ above 600 K.

The precursor likely adsorbed dissociatively on $Ta_xO_y$ at 455 K. Unfortunately the composition could not be determined in this study. Only the demethylation reaction could be detected during TPD.

The low temperature experiments reveal some reactions begin as low as 220 K with the evolution of the *m*/*e* 16 signal in

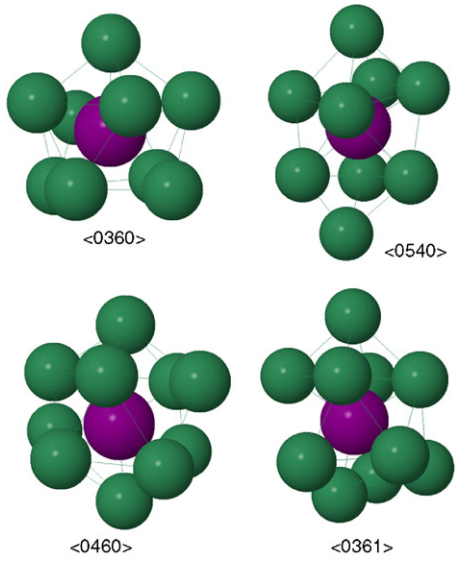


Fig. 16. Calculated coordination polyhedra in the amorphous $Ru_{80}P_{20}$ alloy from *ab initio* molecular dynamics simulations. Large (purple) and small (green) balls represent P and Ru atoms, respectively. (For interpretation of the references to color in this figure legend, the reader is referred to the web version of this article).

TPD. This *m*/*e* 16 signal cannot be associated with methane as it lacks a corresponding *m*/*e* 15 signal and its identity remains unresolved. The relative intensities of the signals during the main 285 K desorption feature in Fig. 13 cannot be accounted for by the precursor and $P(CH_3)_3$ alone. Demethylation contributes to the *m*/*e* 15 signal. The *m*/*e* 76 signal is associated with $P(CH_3)_3$ and a P-containing species whose identity remains unresolved. Finally the trailing edge signals (Fig. 14) reveal the species remaining after molecular desorption continue to undergo demethylation and evolve a P-containing species.

The surface studies illustrate that demethylation is quite efficient near the TPD peak temperature of 560 K (Fig. 10(b)) and this is approximately the minimum temperature for film growth of 525 K. The surface studies also indicate some of the $P(CH_3)_3$ ligands are desorbing, either intact or after partial decomposition, well below the film growth temperature. Therefore, we propose that not all the $P(CH_3)_3$ ligands remain on the surface during growth. Clearly some remain and are directly incorporated into the film. The desorbing P-containing species can also readsorb since the growth pressure is ~26.7 Pa and subsequently incorporate P into the film. This readsorption path could explain why the P content was significantly lower at 525 K than 575 K (Fig. 3). A readsorption path suggests dual sources in which a phosphorus precursor such as $PH_3$, $P(CH_3)_3$ or $P(C_2H_5)_3$ are used along with more conventional Ru precursors could also lead to amorphous Ru–P alloys.

Our *ab initio* MD simulations show the formation of 'quasi-equivalent' P-centered Ru clusters with both topological and chemical short-range order in the $Ru_{80}P_{20}$ amorphous alloy. Subsequently this leads to the medium-range order as the clusters are packed in three-dimensional space. The atomic structure obtained from melt-quenching simulations might differ from that in the experimental samples, whose structure could also be determined by CVD kinetics. Nonetheless, our simulation results clearly demonstrate the existence of amorphous Ru–P alloys with moderate P content.

Films grown at 575 K do feature very small crystalline regions, mostly adjacent to the $SiO_2$ interface. Considering the longer duration at an elevated temperature during deposition and the lower P concentration near the substrate than the surface, it is plausible that Ru atoms organized into small crystallites during the film deposition. These crystallites appear to serve as nucleation centers for the larger crystallites found after annealing to 775 K. Annealing the Ru–P alloy to 775 K and higher demonstrates the films are metastable. Metastability has been reported for other amorphous alloy films [14,16–18]. Modeling and experimental studies are required to establish the extent to which thermodynamically stable compound formation, such as $Ru_2P$ [43], or a more stable alloy composition drive the segregation of the as-grown composition to produce regions that are crystalline and regions that remain amorphous.

## 5. Conclusions

This study reports the CVD growth of a metastable Ru–P alloy at 575 K. Films as thin as 30 nm contain zero-valent Ru and P. The films remain amorphous upon heating for 3 h at 635 K, and begin to crystallize upon annealing at 775 K for 30 min in vacuum. The phosphorus content is related to the growth temperature, with more P found at higher temperatures, and the amount of alklyphosphorus in the chamber background. Separate surface studies suggest the trimethylphosphine ligands undergo demethylation and desorb at the growth conditions and readsorb, and subsequently incorporate the P into the Ru film. Our *ab initio* molecular dynamics study shows that Ru–P alloys with moderate P content can result in glassy structure exhibiting the topological and strong chemical short-range order. In the $Ru_{80}P_{20}$ structure, the P-centered polyhedra prefer the TTP phase with Voronoi index <0,3,6,0>. In addition, the Ru–P system shows the medium-range order arising from packing the "quasi-equivalent" P-centered Ru clusters in three-dimensional space. The structural model based on melt-quenching simulations might differ from that in experimental samples, which could also be determined by CVD kinetics. Nonetheless our simulation results are sufficient to provide invaluable and unique insight into the nature of local packing in Ru–P amorphous structures.

## Acknowledgements

This work was supported by the Semiconductor Research Corporation (Contract 2005-KC-1292.016), the State of Texas Advanced Materials Research Center, and the National Science Foundation (Grant CTS-0553839) and the Robert A. Welch Foundation (Grant F-816).

## References

[1] A. Kaloyeros, X. Chen, K. Kumar, S. Seo, G. Peterson, H. Frisch, B. Arkles, J. Sullivan, J. Electrochem. Soc. 146 (1999) 170.
[2] S. Rossnagel, H. Kim, Proceedings of the IEEE 2001 International Interconnect Technology Conference, Burlingame, U.S.A., June 4–6, 2001, p. 3.
[3] H. Kim, C. Cabral, C. Lavoie, S.M. Rossnagel, J. Vac. Sci. Technol., B 20 (2002) 1321.
[4] S. Kim, S. Oh, H. Kim, D. Kang, K. Kim, W. Li, S. Haukka, M. Tuominen, J. Electrochem. Soc. 151 (2004) C272.
[5] I. Goswami, R. Laxman, Semicond. Int. 27 (2004) 49.
[6] Q. Wang, J.G. Ekerdt, D. Gay, Y. Sun, J.M. White, Appl. Phys. Lett. 84 (2004) 1380.
[7] M. Green, M. Gross, L. Papa, K. Schnoes, D. Brasen, J. Electrochem. Soc. 132 (1985) 2677.
[8] Y. Matsui, M. Hiratani, T. Nabatame, Y. Shimamoto, S. Kimura, Electrochem. Solid-State Lett. 5 (2002) C18.
[9] M. Lashdaf, T. Hatanpää, A.O.I. Krause, J. Lahtinen, M. Lindblad, M. Tiitta, Appl. Catal., A Gen. 241 (2003) 51.
[10] R. Chan, T.N. Arunagiri, Y. Zhang, O. Chyan, R.M. Wallace, M.J. Kim, T.Q. Hurd, Electrochem. Solid-State Lett. 7 (2004) G154.
[11] J. Tan, X. Qu, Q. Xie, Y. Zhou, G. Ru, Thin Solid Films 504 (2006) 231.
[12] H.L. Skriver, N.M. Rosengaard, Phys. Rev., B 46 (1992) 7157.
[13] J. Lin, C. Lee, J. Electrochem. Soc. 146 (1999) 3466.
[14] C.-S. Jun, T.P. Fehlner, Chem. Mater. 4 (1992) 440.
[15] H. Kim, C. Detavenier, O. van der Straten, S.M. Rossnagel, A.J. Kellock, D.-G. Park, J. Appl. Phys. 98 (2005) 014308.
[16] C.M. Eichfeld, M.A. Horsey, S.E. Mohney, A.V. Adedeji, J.R. Williams, Thin Solid Films 485 (2005) 207.
[17] H. Li, H. Li, W. Dai, W. Wang, Z. Fang, J. Deng, Appl. Sur. Sci. 152 (1999) 25.

[18] A. Kohn, M. Eizenberg, Y. Sacham-Diamand, J. Appl. Phys. 94 (2003) 3810.
[19] O.N. Senkov, D.B. Miracle, Mater. Res. Bull. 36 (2001) 2183.
[20] R. Busch, J. Mater. 52 (2000) 39.
[21] J. Basu, S. Ranganathan, Sadhana 28 (Parts 3 & 4) (2003) 783.
[22] L. Xia, S.S. Fang, Q. Wang, Y.D. Dong, C.T. Liu, Appl. Phys. Lett. 88 (2006) 171905.
[23] H.-J. Lee, T. Cagin, W.L. Johnson, W.A. Goddard III, J. Chem. Phys. 119 (2003) 9858.
[24] H.W. Sheng, W.K. Luo, F.M. Alamgir, J.M. Bai, E. Ma, Nature 439 (2006) 419.
[25] H. Schmidbauer, G. Blaschke, Z. Naturforsh. 35b (1980) 584.
[26] W. Kohlmann, H. Werner, Z. Naturforsch. 48b (1993) 1499.
[27] J.P. Perdew, J.A. Chevary, S.H. Vosko, K.A. Jackson, M.R. Pederson, D.J. Singh, C. Fiolhais, Phys. Rev., B 46 (1992) 6671.
[28] G. Kresse, J. Hafner, Phys. Rev., B 47 (1993) 553.
[29] G. Kresse, J. Furthmüller, Comput. Mater. Sci. 6 (1996) 15.
[30] G. Kresse, J. Furthmüller, Phys. Rev., B 54 (1996) 11169.
[31] Y. Lai, Y. Chen, Y. Chi, C. Liu, A.J. Carty, S. Peng, G. Lee, J. Mater. Chem. 13 (2003) 1999.
[32] H. Li, W. Dai, W. Wang, Z. Fang, J. Deng, Appl. Surf. Sci. 152 (1999) 25.
[33] Powder Diffraction File, Joint Committee on Powder Diffraction Standards, ASTM, Philadelphia, PA, 1967 Card 06–0663.
[34] P. Giauque, M. Nicolet, J. Appl. Phys. 93 (2003) 4576.
[35] S. Mader, J. Vac. Sci. Technol. 2 (1964) 35.
[36] C.D. Wagner, L.E. Davis, M.V. Zeller, J.A. Taylor, R.H. Raymond, L.H. Gale, Surf. Interface Anal. 3 (1981) 211.
[37] *Mass Spectra* in NIST Chemistry Webbook, NIST Standard Database Number 69, Eds. P.J. Linstrom and W.G. Mallard, June 2005, NIST, Gaithersburg, MD 20899 (http://webbook.nist.gov).
[38] J.L. Pinney, Proc. R. Soc. A 319 (1970) 479.
[39] J.L. Pinney, Nature 266 (1977) 309.
[40] Y. Qi, T. Cagin, Y. Kimura, W.A. Goddard III, Phys. Rev., B 59 (1999) 3527.
[41] D. Duan, D. Xu, Q. Zhang, Q. Zhang, T. Cagin, W.L. Johnson, W.A. Goddard III, Phys. Rev., B 71 (2005) 224208.
[42] H.-S. Tao, U. Diebold, N.D. Shinn, T.E. Madey, Surf. Sci. 375 (1997) 257.
[43] V.B. Chernogorenko, V.G. Ivanchenko, L. Ya. Kulik, in: T.B. Massalski, H. Okamoto, P.R. Subramanian, L. Kacprzak (Eds.), Binary Phase Diagrams, ASM International, Materials Park, 1990, p. 2979.